



# A Single Particle Model for Lithium-Ion Batteries with Electrolyte and Stress-Enhanced Diffusion Physics

J. Li, N. Lotfi, R. G. Landers, and J. Park<sup>2</sup>

Department of Mechanical and Aerospace Engineering, Missouri University of Science and Technology, Rolla, Missouri 65401, USA

A low-order battery model has been developed that incorporates stress-enhanced diffusion and electrolyte concentration distribution into a modified single particle model. This model addresses two important challenges of battery modeling for Battery Management Systems: accuracy and computational efficiency. The developed model improves accuracy by including the potential drop in the electrolyte based on the predicted li-ion concentration profile along the entire electrode thickness, and by including the enhanced diffusivity due to diffusion-induced stress. Incorporating analytical solutions into a conventional single particle model eliminates the need to sacrifice calculation efficiency. The voltage prediction by the proposed model is more accurate than the conventional single particle model. Compared to complex physics-based battery models, the proposed model significantly improves the computational efficiency of various discharge scenarios, including constant current, the Dynamic Stress Test, and the Highway Fuel Economy Test. Integrating mechanical responses into the single particle model not only increases model accuracy, but also makes it applicable to models for next-generation high energy density materials where mechanical volume changes are important.

© 2017 The Electrochemical Society. [DOI: [10.1149/2.1541704jes](https://doi.org/10.1149/2.1541704jes)] All rights reserved.

Manuscript submitted December 5, 2016; revised manuscript received January 23, 2017. Published February 28, 2017.

Lithium Ion Batteries (LIBs) have the advantages of higher energy and power density, as compared to other rechargeable batteries, and are presently regarded as a core technology for energy storage and supply for Electric Vehicles (EV) and Hybrid Electric Vehicles (HEV).<sup>1,2</sup> However, as the usage of LIBs becomes more pervasive, increased concerns about their safety has become more critical. Consequently, a Battery Management System (BMS) is used to optimize storage capacity and balance the various systems to satisfy functional requirements and prevent catastrophic failures.<sup>3,4</sup> In order to achieve these goals through a BMS, identification of the battery status is extremely important.<sup>5</sup> Therefore, advanced sensing and monitoring technologies are required to accurately predict the state of the battery and track the physical parameters. However, current sensing and monitoring technologies that rely heavily on voltage, current, and temperature are not sufficient to accurately predict the batteries' State of Charge (SOC) and State of Health (SOH). For this reason, a battery physical model is typically used in battery control and management systems, so that the internal battery status can be determined more accurately.<sup>6-9</sup> High-fidelity electrochemical models are ideal for detailed analysis of battery phenomena, but are too computationally intensive to use efficiently in BMS.<sup>3</sup> This has led to efforts to reduce the complexity of the electrochemical battery models. For example, the electrochemical model that was proposed by Doyle et al.<sup>10</sup> was reduced to a form suitable for a BMS.<sup>3,11,12</sup> However, for those simplified models, the process of identifying the model parameters, which is needed to construct these models, is difficult. One well-known simplified model is the Equivalent Circuit Model (ECM), which describes battery dynamic behavior as a voltage source and a series of resistors and capacitors.<sup>13</sup> The common method for identifying ECM parameters is to use tests such as the Hybrid Power Pulse Characterization (HPPC) test.<sup>14</sup> However, these tests suffer from excessive measurement noise and lack of accurate initial estimates.<sup>15</sup> Most of all, the ECM model has limited prediction capability as it does not consider the electrochemical phenomena behind the battery performance.<sup>16</sup> The Single Particle (SP) model strikes the necessary balance between the electrochemical and equivalent circuit models. The SP model is described by a small series of ordinary differential equations, but it is derived directly from comprehensive electrochemical models, so it maintains many important battery characteristics explicitly. The SP model assumes that both electrodes are composed of spherical particles of the same shape and size, and the current distribution is uniform across both electrodes. Thus, each electrode can

be approximated by a single spherical particle. The mass balance of li-ions in the intercalated particles of the electrode active material is described by Fick's law. One important drawback of the SP model is that it does not adequately describe the battery dynamics at high C-rates due to the absence of the electrolyte physics, even though it adequately describes the general charge-discharge behavior of the battery.<sup>16-20</sup>

In order to overcome this challenge, different approximations have been proposed for coupling the SP model with the electrolyte contribution by using different polynomial equations with various orders.<sup>21-25</sup> In general, the polynomial order determines the accuracy of the approximation. Higher-order polynomials will result in a higher accuracy; however, the numerical cost of the coefficient identification scheme will increase accordingly. A quadratic equation describing the electrolyte concentration in the electrodes with a maximum error of approximately 4~8% was used in the Refs. 22 and 25. Rahmian et al.<sup>23</sup> reported a high charging rate with optimized pore wall flux using a third order polynomial for the electrolyte concentration in the electrodes. This model showed a maximum error of approximately 4% for a 5 C discharge using a volume averaged flux. In addition, Naoki et al.<sup>24</sup> studied battery thermal behavior using an SP model with electrolyte concentrations described by a parabolic profile. These models have shown improvement by adding the electrolyte physic model, but they are still not accurate (2~4% maximum error) compared to full-order electrochemical models. Further, some equations in the model were cumbersome and complicated for BMS applications.

Battery materials are inherently mechanical systems, where large and repeated strains develop inside the materials, and the corresponding stresses lead to cracks and fractures.<sup>26-32</sup> The basic function of electrochemical materials is fulfilled by ions' intercalating into the materials, meaning the ions enter the materials due to an electrochemical potential gradient.<sup>32</sup> During this intercalation process, there is a typical volume change of 10% for commercially available graphite materials, and even up to 300% for silicon materials.<sup>27,33</sup> This volume change causes considerable stress inside the materials, leading to mechanical failures, such as material pulverization, and cracks and fractures in the materials. Further, the stress field inside a particle affects the diffusion process of li-ions. As a li-ion intercalates into the host material, a stress field builds due to displacement of the host atoms caused by the intercalated ion. This stress field affects the energy of the second intercalated ion, leading to an elastic interaction between the two ions. This means that the diffusion process of ions in a particle under stress field is different from the stress-free diffusion behavior. Accordingly, these mechanical responses must be integrated into the SP model to

<sup>2</sup>E-mail: [parkjonghy@mst.edu](mailto:parkjonghy@mst.edu)

determine the precise diffusivity of ions and their internal battery physics. It is also essential to predict the mechanical failure of battery electrodes.

In this study, we propose a new SP model that include electrolyte physics and a stress-diffusion coupling effect that improves the accuracy and computational efficiency of conventional SP models. To this end, a second-order analytical expression for electrolyte concentration distribution was developed based on electrochemical physics inside the entire battery cell, and the stress-enhanced diffusion was coupled to these physics. Simulation results of the proposed SP model were validated by comparing them with the results from a full-order electrochemical model and a conventional SP model. Further, galvanostatic constant discharge tests, the Dynamic Stress Test (DST), and the Highway Fuel Economy Test (HWFET) were conducted to demonstrate the accuracy of the new SP model for various operation scenarios.

### Proposed Single Particle Model with Electrolyte and Stress-Enhanced Diffusion Physics

Figure 1 is a schematic of a li-ion cell composed of two electrodes (solid matrix inside an electrolyte solution) and a separator (electrolyte solution). In the full order Pseudo-2D (P2D) electrochemical model, li-ion transport in the electrolyte phase is considered only in the  $x$  direction. The diffusional process in the solid phase is solved based on a symmetric spherical particle assumption that the electrochemical reaction takes place on the surface of the particle.

The P2D electrochemical battery model consists of ten coupled nonlinear partial differential equations for the mass and charge balance in the solid and electrolyte phases.<sup>12</sup> The SP model is a simplified form of the P2D model; however, it does not include the electrolyte physics and mechanical responses. The following section presents the governing equations and assumptions for the proposed SP model.

**Single particle model.**—In the conventional SP model, it is assumed that all particles in the electrode behave in a similar manner. Therefore, each electrode can be modeled as a single spherical particle, as shown in Fig. 1. Further, current passing through an electrode is assumed to be distributed uniformly over all of the particles.<sup>18,34</sup> Each li-ion travels inside spherical solid particles by a diffusion process given by Fick's second law

$$\frac{\partial c_{s,j}(r,t)}{\partial t} = \frac{D_{s,j}}{r^2} \frac{\partial}{\partial r} \left[ r^2 \frac{\partial c_{s,j}(r,t)}{\partial r} \right] \quad [1]$$

where  $c_{s,j}$  is the solid-phase li-ion concentration,  $t$  is time,  $r$  is the radial coordinate,  $D_{s,j}$  is the solid-phase diffusion coefficient, and the subscript  $j = p/n$  denotes the positive/negative electrode.

The boundary conditions for Eq. 1 are

$$D_{s,j} \frac{\partial c_{s,j}(r,t)}{\partial r} \Big|_{r=0} = 0, \quad D_{s,j} \frac{\partial c_{s,j}(r,t)}{\partial r} \Big|_{r=R_j} = -J^{Li} \quad [2]$$

where  $R_j$  is the electrode particle radius.

The electrochemical reaction rate for the li-ion intercalation/(de)intercalation at the solid/solution interface,  $J^{Li}$ , can be expressed via the Butler-Volmer kinetics as<sup>34</sup>

$$J^{Li} = k_j c_{s,j,max} c_e^{0.5} \left[ 1 - \frac{c_{s,j,surf}(t)}{c_{s,j,max}} \right]^{0.5} \left( \frac{c_{s,j,surf}(t)}{c_{s,j,max}} \right)^{0.5} \times \left\{ \exp \left[ \frac{0.5F}{RT} \eta_j(t) \right] - \exp \left[ -\frac{0.5F}{RT} \eta_j(t) \right] \right\} \quad [3]$$

where  $k_j$  is the reaction rate constant,  $c_e$  is the electrolyte concentration,  $R$  is the universal gas constant,  $T$  is the temperature,  $F$  is Faraday's constant, and  $c_{s,j,surf}(t)$  is expressed as a function of particle surface concentration  $c_{s,j,surf}(t) = c_{s,j}(R_j, t)$ .

The parameter  $\eta_j$  is the surface over-potential, defined as  $\eta_j = \Phi_{1,j} - \Phi_{2,j} - U_j$ , where  $\Phi_{1,j}$  is the solid-phase potential,  $\Phi_{2,j}$  is solution-phase potential, and  $U_j$  is the Open Circuit Potential (OCP). The OCP, in general, is a function of the normalized surface concentration,  $c_{s,j,surf}(t)/c_{s,j,max}(t)$ , and temperature. Then, the potential difference can be obtained from Eq. 3

$$\eta_j(t) = \frac{2RT}{F} \ln \left[ m_j(t) + \sqrt{m_j^2(t) + 1} \right] \quad [4]$$

$$\text{where } m_j(t) = \frac{J^{Li}}{2k_j c_{s,j,max} c_e^{0.5} \left[ 1 - \frac{c_{s,j,surf}(t)}{c_{s,j,max}} \right]^{0.5} \left( \frac{c_{s,j,surf}(t)}{c_{s,j,max}} \right)^{0.5}}.$$

Finally, the li-ion battery terminal voltage can be calculated based on the solid phase potential difference between both ends of the cell<sup>34</sup>

$$\begin{aligned} V_t(t) &= \Phi_{1,p}(t)|_{x=L} - \Phi_{1,n}(t)|_{x=0} \\ &= (\eta_p + \Phi_{2,p}(t)|_{x=L} + U_p) - (\eta_n + \Phi_{2,n}(t)|_{x=0} + U_n) \\ &= U_p \left[ \frac{c_{s,p,surf}(t)}{c_{s,p,max}} \right] - U_n \left[ \frac{c_{s,n,surf}(t)}{c_{s,n,max}} \right] \\ &\quad + \frac{2RT}{F} \left\{ \ln \left[ m_p(t) + \sqrt{m_p^2(t) + 1} \right] \right. \\ &\quad \left. - \ln \left[ m_n(t) + \sqrt{m_n^2(t) + 1} \right] \right\} + \Phi_{2,p}(t)|_{x=L} - \Phi_{2,n}(t)|_{x=0} \end{aligned} \quad [5]$$

where  $\Phi_{2,p}(t)|_{x=L} - \Phi_{2,n}(t)|_{x=0}$  denotes the electrolyte potential difference.

In SP models, the potential gradient inside the electrolyte is neglected. In such models, introducing a resistance term into the Butler-Volmer kinetics only aims at modeling the interface resistance and does not account for the potential distribution within the electrolyte. The internal resistance is approximated as an ohmic voltage drop,  $i_{app} R_{cell}$ , where  $i_{app}$  is the applied current density. The resistance value  $R_{cell}$  depends on many complex mass and charge transfer phenomena. Guo et al.<sup>34</sup> approximated this resistance as an empirical function of the ambient temperature and the battery terminal current. In Ref. 35, the resistance  $R_{cell}$  is assumed as a function of electrode ionic conductivities and electrode thicknesses. This assumption is a critical drawback of the conventional SP model and, as a result, the model cannot adequately describe battery dynamics at high C-rates.<sup>16–20</sup>

**Electrolyte concentration distribution and electrolyte potential difference.**—In the proposed SP model, the li-ion concentration distribution is obtained by applying mass conservation in the electrolyte. Here, the electrolyte concentration distribution,  $c_{e,i}(x,t)$ , includes the

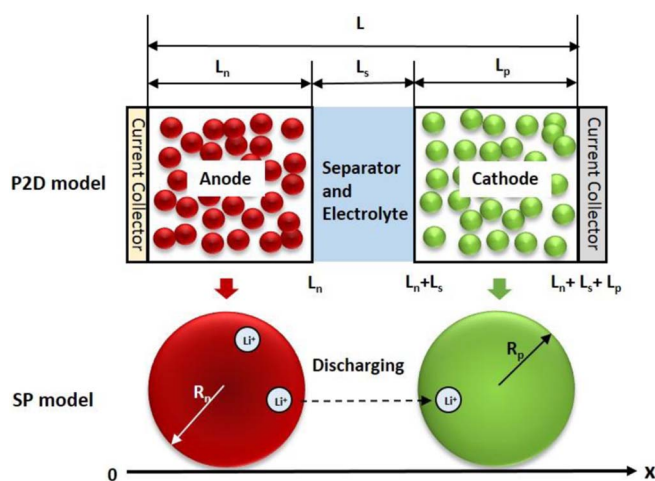


Figure 1. Schematic representation of three regions in li-ion cell.

lithium ionic concentration in both electrodes and the separator as a function of time,  $t$ , and position,  $x$ , where the subscript  $i = p/s/n$  represents the positive electrode/separator/negative electrode. The transfer of li-ions in the electrolyte can be described by porous electrode theory. In the separator region, Fick's first law is used because there is no electrochemical reaction in that region. Consequently, the governing equations for the electrolyte concentration in the positive electrode, separator, and negative electrode, respectively, are<sup>22,25</sup>

$$\varepsilon_{e,n} \frac{\partial c_{e,n}}{\partial t} = D_{e,n}^{eff} \frac{\partial^2 c_{e,n}}{\partial x^2} + (1 - t_+) \frac{i_{app}}{FL_n} \quad (0 \leq x \leq L_n) \quad [6]$$

$$\varepsilon_{e,s} \frac{\partial c_{e,s}}{\partial t} = D_{e,s}^{eff} \frac{\partial^2 c_{e,s}}{\partial x^2} \quad (L_n \leq x \leq L_n + L_s) \quad [7]$$

$$\varepsilon_{e,p} \frac{\partial c_{e,p}}{\partial t} = D_{e,p}^{eff} \frac{\partial^2 c_{e,p}}{\partial x^2} + (1 - t_+) \frac{i_{app}}{FL_p} \quad (L_n + L_s \leq x \leq L_n + L_s + L_p) \quad [8]$$

where  $D_{e,i}^{eff} = D_e \varepsilon_{e,i}^{brug}$  is the effective diffusivity,  $L_n/L_s/L_p$  and  $\varepsilon_{e,n}/\varepsilon_{e,s}/\varepsilon_{e,p}$  are the thicknesses and the porosities for the anode, separator, and cathode, respectively, and *brug* denotes the bruggeman coefficient, which is 1.5.

The diffusion coefficient,  $D_e$ , and the cationic transport number in the electrolyte,  $t_+$ , are considered to be constant and independent of the electrolyte concentration. Considering the continuity of the concentration and mass flux, their boundary conditions can be expressed as:

1. No mass flux at the two ends of the cell in the  $x$ -direction

$$\left. \frac{\partial c_{e,n}}{\partial x} \right|_{x=0} = 0, \quad \left. \frac{\partial c_{e,p}}{\partial x} \right|_{x=L} = 0 \quad [9]$$

2. Continuity of the concentration and flux at the anode-separator interface

$$c_{e,n}(L_n, t) = c_{e,s}(L_n, t), \quad D_{e,n}^{eff} \left. \frac{\partial c_{e,n}}{\partial x} \right|_{x=L_n} = D_{e,s}^{eff} \left. \frac{\partial c_{e,s}}{\partial x} \right|_{x=L_n} \quad [10]$$

3. Continuity of the concentration and flux at the separator-cathode interface

$$c_{e,s}(L_n + L_s, t) = c_{e,p}(L_n + L_s, t), \quad D_{e,s}^{eff} \left. \frac{\partial c_{e,s}}{\partial x} \right|_{x=L_n+L_s} = D_{e,p}^{eff} \left. \frac{\partial c_{e,p}}{\partial x} \right|_{x=L_n+L_s} \quad [11]$$

4. Electrolyte concentration balance inside the entire region

$$\int_0^{L_n} c_{e,n}(x, t) \varepsilon_{e,n} dx + \int_{L_n}^{L_n+L_s} c_{e,s}(x, t) \varepsilon_{e,s} dx + \int_{L_n+L_s}^{L_n+L_s+L_p} c_{e,p}(x, t) \varepsilon_{e,p} dx = c_0 (L_n + L_s + L_p) \quad [12]$$

The continuous electrolyte concentration profiles (Eqs. 6–8) can be approximated, in general, by polynomial functions

$$c_{e,i}(x, t) = \alpha_k(t) x^m + \alpha_k(t) x^{m-1} \dots + \alpha_k(t) + \beta \quad [13]$$

$i = p, s, n \quad k = 1, 2, 3 \dots$

The polynomial orders for the electrolyte concentrations in the electrodes and separator can be different. It has been observed at steady state that the electrolyte concentration distribution can be approximated by a parabolic profile in the electrodes and a linear profile in the separator.<sup>22</sup> At the beginning of discharge, the li-ions deintercalate from the active particles to the electrolyte in the negative electrode, and intercalate from the electrolyte to the cathode parti-

cles in the positive electrode. Thus, the electrolyte concentration in the negative electrode increases, while it decreases in the positive electrode. As  $t = \infty$ , the cell stays a steady status and the competitive effects of the li-ions moving into/out of the electrolyte from the solid electrodes (i.e. electrochemical reaction) and the concentration gradient (i.e. diffusion) are balanced.<sup>22,23</sup> In this work, second-order polynomials are chosen for the electrolyte concentrations inside the negative electrode, the separator, and the positive electrode, respectively. For this, the general equation in Eq. 13 is further simplified with  $\alpha_k$  as a form of  $a_k(1 - e^{-b_k t})$  and  $\beta$  to be the initial concentration  $c_0$

$$c_{e,n}(x, t) = a_1(1 - e^{-b_1 t})x^2 + a_2(1 - e^{-b_1 t}) + c_0 \quad [14]$$

$$c_{e,s}(x, t) = a_3(1 - e^{-b_3 t})x^2 + a_4(1 - e^{-b_3 t}) + c_0 \quad [15]$$

$$c_{e,p}(x, t) = a_5(1 - e^{-b_2 t})(L - x)^2 + a_6(1 - e^{-b_2 t}) + c_0 \quad [16]$$

The initial electrolyte concentration is

$$c_{e,i}(x, 0) = c_0 \quad [17]$$

Under steady-state conditions, the electrolyte concentrations at different locations are independent of time; therefore, Equations 14–16, respectively, become

$$c_{e,n}(x, t) = a_1 x^2 + a_2 + c_0 \quad [18]$$

$$c_{e,s}(x, t) = a_3 x^2 + a_4 + c_0 \quad [19]$$

$$c_{e,p}(x, t) = a_5(L - x)^2 + a_6 + c_0 \quad [20]$$

In addition, based on Eqs. 6–8, the total amount of  $\text{Li}^+$  in the three regions can be expressed by the following equations:<sup>25</sup>

$$\frac{d}{dt} \left( \varepsilon_{e,n} \int_0^{L_n} c_{e,n}(x, t) dx \right) = D_{e,n}^{eff} \frac{dc_{e,n}(L_n, t)}{dx} + (1 - t_+) \frac{i_{app}}{F} \quad [21]$$

$$\begin{aligned} \frac{d}{dt} \left( \varepsilon_{e,s} \int_{L_n}^{L_n+L_s} c_{e,s}(x, t) dx \right) \\ = D_{e,s}^{eff} \left( \frac{dc_{e,s}(L_n + L_s, t)}{dx} - \frac{dc_{e,s}(L_n, t)}{dx} \right) \end{aligned} \quad [22]$$

$$\begin{aligned} \frac{d}{dt} \left( \varepsilon_{e,p} \int_{L_n+L_s}^{L_n+L_s+L_p} c_{e,p}(x, t) dx \right) \\ = -D_{e,p}^{eff} \frac{dc_{e,p}(L_n + L_s, t)}{dx} - (1 - t_+) \frac{i_{app}}{F} \end{aligned} \quad [23]$$

The coefficients  $a_k$  can be obtained from the boundary conditions in Eqs. 10–12 and from mass conservation (Eqs. 21–23)

$$a_1 = -\frac{\varepsilon_{e,n}^{-brug} J}{2D_e L_n} \quad [24]$$

$$a_2 = \frac{\{J[\varepsilon_{e,n}^{1-brug} L_n^2 + 2\varepsilon_{e,p}^{1-brug} L_p^2 + 6\varepsilon_{e,p}\varepsilon_{e,s}^{-brug} L_s L_p + 3\varepsilon_{e,s}^{1-brug} L_s^2 + 3\varepsilon_{e,n}^{1-brug} L_n(\varepsilon_{e,p} L_p + \varepsilon_{e,s} L_s)]\}}{6D_e(\varepsilon_{e,n} L_n + \varepsilon_{e,p} L_p + \varepsilon_{e,s} L_s)} \quad [25]$$

$$a_5 = \frac{\varepsilon_{e,p}^{-brug} J}{2D_e L_p} \quad [26]$$

$$a_6 = -\frac{J(2\varepsilon_{e,n}^{1-brug} L_n^2 + 3\varepsilon_{e,n}\varepsilon_{e,p}^{-brug} L_n L_p + \varepsilon_{e,p}^{1-brug} L_p^2 + 6\varepsilon_{e,n}\varepsilon_{e,s}^{-brug} L_n L_s + 3\varepsilon_{e,p}^{-brug} \varepsilon_{e,s} L_s L_p + 3\varepsilon_{e,s}^{1-brug} L_s^2)}{6D_e(\varepsilon_{e,n} L_n + \varepsilon_{e,p} L_p + \varepsilon_{e,s} L_s)} \quad [27]$$

where  $J = (1 - t_+) \frac{i_{app}}{F}$ .

In the unsteady state, a linear concentration in the separator is assumed to simplify Eq. 15 using two values at the boundaries of the anode-separator and separator-cathode. As a result, the expression for electrolyte concentration distribution in the separator (Eq. 15) can be rewritten as

$$c_{e,s}(x, t) = \frac{(x - L_n - L_s) \{a_5(1 - e^{-b_2 t}) L_p^2 + a_6(1 - e^{-b_2 t}) - [a_1(1 - e^{-b_1 t}) L_n^2 + a_2(1 - e^{-b_1 t})]\}}{L_s} + a_5(1 - e^{-b_2 t}) L_p^2 + a_6(1 - e^{-b_2 t}) + c_0 \quad [28]$$

Then, based on flux continuity and approximated solution (Eqs. 10, 11, 14, 16 and 28), the coefficients  $b_1$  and  $b_2$  are

$$b_1 = \frac{6D_e \varepsilon_{e,n}^{brug-1} \varepsilon_{e,p}^{brug} \varepsilon_{e,s}^{brug} (\varepsilon_{e,n} L_n + \varepsilon_{e,p} L_p + \varepsilon_{e,s} L_s)}{L_n \left[ 2\varepsilon_{e,n}^{brug} \varepsilon_{e,p}^{brug} \varepsilon_{e,s}^{brug} L_p^2 + 2\varepsilon_{e,p}^{1+brug} L_p (\varepsilon_{e,s}^{brug} L_n + 3\varepsilon_{e,n}^{brug} L_s) + \varepsilon_{e,p}^{brug} \varepsilon_{e,s} L_s (2\varepsilon_{e,s}^{brug} L_n + 3\varepsilon_{e,n}^{brug} L_s) \right]} \quad [29]$$

$$b_2 = \frac{6D_e \varepsilon_{e,n}^{brug} \varepsilon_{e,p}^{brug-1} \varepsilon_{e,s}^{brug} (\varepsilon_{e,n} L_n + \varepsilon_{e,p} L_p + \varepsilon_{e,s} L_s)}{L_p \left[ 2\varepsilon_{e,n}^{brug} \varepsilon_{e,p}^{brug} \varepsilon_{e,s}^{brug} L_n^2 + 2\varepsilon_{e,n}^{1+brug} L_n (\varepsilon_{e,s}^{brug} L_p + 3\varepsilon_{e,p}^{brug} L_s) + \varepsilon_{e,n}^{brug} (2\varepsilon_{e,s}^{1+brug} L_p L_s + 3\varepsilon_{e,p}^{brug} \varepsilon_{e,s} L_s^2) \right]} \quad [30]$$

Eqs. 14, 16, and 28 are the analytical solutions for the electrolyte concentration distribution in the cathode, electrolyte, and anode regions, respectively, as a function of the spatial coordinate  $x$  (Fig. 1).

Then the electrolyte potential and potential difference can be calculated as detailed in Ref. 36. The analytical equations for electrolyte potential were derived based on the electrolyte charge conservation equation, and expressed as:

For the negative electrode region ( $0 \leq x \leq L_n$ )

$$\Phi_e(x) = \Phi_e(0) + (1 - t_+) \frac{2RT}{F} \ln \frac{c_e(x)}{c_e(0)} - \frac{i_{app}}{2L_n k_n^{eff}} x^2 \quad [31]$$

For the separator region ( $L_n \leq x \leq L_n + L_s$ )

$$\Phi_e(x) = \Phi_e(0) + (1 - t_+) \frac{2RT}{F} \ln \frac{c_e(x)}{c_e(0)} - \frac{i_{app}}{k_s^{eff}} (x - L_n) - \frac{i_{app} L_n}{2k_n^{eff}} \quad [32]$$

For the positive electrode region ( $L_n + L_s \leq x \leq L_n + L_s + L_p$ )

$$\Phi_e(x) = \Phi_e(0) + (1 - t_+) \frac{2RT}{F} \ln \frac{c_e(x)}{c_e(0)} + \frac{i_{app}}{2L_p k_p^{eff}} (L - x)^2 - \frac{i_{app}}{2} \left( \frac{L_n}{k_n^{eff}} + \frac{2L_s}{k_s^{eff}} + \frac{L_p}{k_p^{eff}} \right) \quad [33]$$

where  $k_i^{eff} = k_i * \varepsilon_i^{brug}$ , and  $k_n$ ,  $k_s$ , and  $k_p$  are the electrolyte conductivities in the anode, separator, and cathode, respectively, which are functions of electrolyte concentration.<sup>36</sup>

The electrolyte potential difference is obtained by the difference between the potentials taken from the electrode-current collector interface (i.e.,  $x = 0$  and  $x = L$ ). In addition, the last part of Eq. 34 can be regarded as an ohmic resistance, which is expressed as a function

of electrode geometry and electrolyte effective conductivity<sup>36</sup>

$$\begin{aligned} \Phi_{2,p}(t)|_{x=L} - \Phi_{2,n}(t)|_{x=0} &= \Phi_e(L, t) - \Phi_e(0, t) \\ &= (1 - t_+) \frac{2RT}{F} \ln \frac{c_{e,p}(L, t)}{c_{e,n}(0, t)} - \frac{i_{app}}{2} \left( \frac{L_n}{k_n^{eff}} + \frac{2L_s}{k_s^{eff}} + \frac{L_p}{k_p^{eff}} \right) \end{aligned} \quad [34]$$

**Stress model.**—In order to calculate the solid phase li-ion concentration due to a stress buildup, the insertion/extraction of ions are modeled as a diffusion-stress coupling process. By considering the chemical potential due to the concentration gradient and mechanical strain energy,<sup>28</sup> the species flux,  $J_{st}$ , can be expressed by

$$J_{st} = -D_{s,j} \left[ \nabla c_{s,j}(r, t) - \frac{\Omega_j c_{s,j}(r, t)}{RT} \nabla \sigma_h \right] = \frac{i_{app}}{F} \quad [35]$$

$$\frac{\partial c_{s,j}(r, t)}{\partial t} + \nabla \cdot J_{st} = 0 \quad [36]$$

where  $\Omega_j$  is the partial molar volume and  $\sigma_h$  is the hydrostatic stress. Substituting Eq. 35 into Eq. 36,

$$\begin{aligned} \frac{\partial c_{s,j}(r, t)}{\partial t} &= D_{s,j} \left[ \nabla^2 c_{s,j}(r, t) - \frac{\Omega_j}{RT} \nabla c_{s,j}(r, t) \cdot \nabla \sigma_h \right. \\ &\quad \left. - \frac{\Omega_j c_{s,j}(r, t)}{RT} \nabla^2 \sigma_h \right] \end{aligned} \quad [37]$$



For the case of a spherical particle, the stress tensor contains two independent components:<sup>28</sup> radial stress  $\sigma_r$  and tangential stress  $\sigma_t$ .

$$\sigma_r = \frac{2\Omega_j E_j}{3(1-\nu_j)} \left( \frac{1}{R_j^3} \int_0^{R_j} \tilde{c} r^2 dr - \frac{1}{r^3} \int_0^r \tilde{c} r^2 dr \right) \quad [38]$$

$$\sigma_t = \frac{\Omega_j E_j}{3(1-\nu_j)} \left( \frac{2}{R_j^3} \int_0^{R_j} \tilde{c} r^2 dr - \frac{1}{r^3} \int_0^r \tilde{c} r^2 dr - \tilde{c} \right) \quad [39]$$

where  $\tilde{c}$  is the concentration change from the initial value,  $\nu_j$  is the Poisson's ratio, and  $E_j$  is the Young's modulus of active materials. The hydrostatic stress is<sup>28</sup>

$$\sigma_h = (\sigma_r + 2\sigma_t)/3 = \frac{2\Omega_j E_j}{9(1-\nu_j)} \left( \frac{3}{R_j^3} \int_0^{R_j} \tilde{c} r^2 dr - \tilde{c} \right) \quad [40]$$

Substituting Eq. 40 into Eqs. 35 and 37,

$$\frac{\partial c_{s,j}(r,t)}{\partial t} = D \left[ \frac{\partial^2 c_{s,j}(r,t)}{\partial r^2} + \frac{2}{r} \frac{\partial c_{s,j}(r,t)}{\partial r} + \theta_j \left( \frac{\partial c_{s,j}(r,t)}{\partial r} \right)^2 + \theta_j c \left( \frac{\partial^2 c_{s,j}(r,t)}{\partial r^2} + \frac{2}{r} \frac{\partial c_{s,j}(r,t)}{\partial r} \right) \right] \quad [41]$$

$$J_{st} = -D_{s,j} (1 + \theta_j c_{s,j}(r,t)) \frac{\partial c_{s,j}(r,t)}{\partial r} \quad \text{at } r = R_j \quad [42]$$

where  $\theta_j = \frac{2\Omega_j^2 E_j}{9RT(1-\nu_j)}$ . Eqs. 1 and 2 are replaced by Eqs. 41 and 42, respectively, in the proposed SP model to calculate the solid phase concentration, and  $J^{Li}$  is replaced with  $J_{st}$  in Eq. 3. In this way, the stress model is coupled with the proposed SP model with accurate electrolyte physics.

## Results and Discussion

In order to demonstrate the effectiveness of the proposed model, the  $\text{LiMn}_2\text{O}_4\text{-LiC}_6$  battery chemistry from Doyle et al.<sup>10</sup> was adopted in this work. The parameters used in the simulation are listed in Table I. All of the models were simulated on a computer using the Windows operating system with a 1.9 GHz Intel Xeon CPU and 24 GB of RAM. The P2D model (denoted "P2D"), conventional SP model (denoted "SP"), and proposed SP model (denoted "proposed model") with/without stress consideration were simulated in Matlab with a COMSOL-Matlab LiveLink function. The computation time was recorded via a Time Portions of Code in Matlab. Each model used the same sampling period (1 s) and a 1 C discharge rate for 2810 s (4.2 V to 3 V) to compare the computational efficiency. The Matlab program execution times for each model are listed in Table II. The computational time of the SP model (19.0 s) and the proposed model (19.2 s) were reduced by 65%, as compared to the P2D model (55.0 s). In addition, when the stress field is added, the computational time of the P2D and the proposed SP models increases by 14 s and 3.1 s, respectively. The proposed SP shortens the time of the P2D by 68%.

**Electrolyte concentration distribution and electrolyte potential difference.**—In order to verify the proposed model, the electrolyte concentration distributions of the analytical equations (Eqs. 14, 16 and 28) were compared with the numerical solutions of the governing equations with the boundary conditions given in Eqs. 6–12, and 17. The results of the electrolyte concentration distribution are shown in Fig. 2a. Using the parameters in Table I, the concentration change for a 1 C discharge is displayed in Fig. 2a as a function of position,  $x$ , at different times,  $t$ . The prediction error between the second-order analytical equations and the P2D model is a result of reduced degrees of freedom in the empirical equation for the electrolyte concentration. In addition, the accuracy of the proposed model increased over time (0.82% maximum error at 30 s to 0.36% maximum error at 1500 s)

**Table I. Values of parameters used in the simulations.**

Parameter	Value	Description	Ref
$L_n$	$1 \times 10^{-4}$	Thickness of the negative electrode (m)	10
$L_s$	$52 \times 10^{-6}$	Thickness of the separator (m)	10
$L_p$	$183 \times 10^{-6}$	Thickness of the positive electrode (m)	10
$\varepsilon_n$	0.375	Porosity of the negative electrode	10
$\varepsilon_s$	1	Porosity of the separator	10
$\varepsilon_p$	0.444	Porosity of the positive electrode	10
$D_e$	$7.5 \times 10^{-11}$	Diffusion coefficient in electrolyte ( $\text{m}^2\text{s}^{-1}$ )	10
$k_j$	$2 \times 10^{-6}$	Reaction rate constant ( $\text{m}^{2.5}\text{mol}^{-0.5}\text{s}^{-1}$ )	10
$F$	96487	Faraday's constant ( $\text{C mol}^{-1}$ )	10
$t_+$	0.363	Cationic transport number	10
$i_{app}$	$17.5 \times \text{C-rate}$	C-rate times 1 C discharge current density ( $\text{A m}^{-2}$ )	10
$c_0$	2000	Initial concentration ( $\text{mol m}^{-3}$ )	10
$D_{s,n}$	$3.9 \times 10^{-14}$	Solid-phase Li diffusivity, negative electrode ( $\text{m}^2\text{s}^{-1}$ )	10
$D_{s,p}$	$1 \times 10^{-13}$	Solid-phase Li diffusivity, positive electrode ( $\text{m}^2\text{s}^{-1}$ )	10
$R_n$	$12.5 \times 10^{-6}$	Particle radius, negative electrode (m)	10
$R_p$	$8 \times 10^{-6}$	Particle radius, positive electrode (m)	10
$R$	8.314	Universal gas constant ( $\text{J mol}^{-1} \text{K}^{-1}$ )	10
$T$	298.15	Ambient temperature (K)	10
$E_s$	10	LMO Young's modulus (GPa)	55
$E_n$	60	LiC <sub>6</sub> Young's modulus (GPa)	33
$\nu_s$	0.3	LMO Poisson's ratio	55
$\nu_n$	0.25	LiC <sub>6</sub> Poisson's ratio	33
$\Omega_s$	$3.499 \times 10^{-6}$	LMO partial molar volume	26
$\Omega_n$	$4.926 \times 10^{-6}$	LiC <sub>6</sub> partial molar volume	26
$C_{\max, pos}$	22860	Positive maximum concentration ( $\text{mol m}^{-3}$ )	10
$C_{\max, neg}$	26390	Negative maximum concentration ( $\text{mol m}^{-3}$ )	10

**Table II. Comparison of P2D model, SP model, and proposed model computation times for 1 C discharge.**

Model	Computation time (s)	
	without stress consideration	with stress consideration
P2D	55.0	69.0
SP	19.0	22.0
Proposed model	19.2	22.3

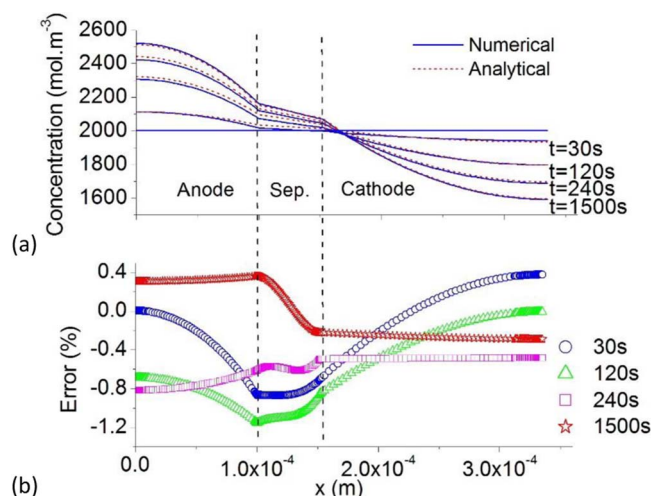


**Figure 2.** (a) Comparison of the electrolyte concentration distribution at different times for a 1 C discharge rate, (b) percentile errors between solutions.

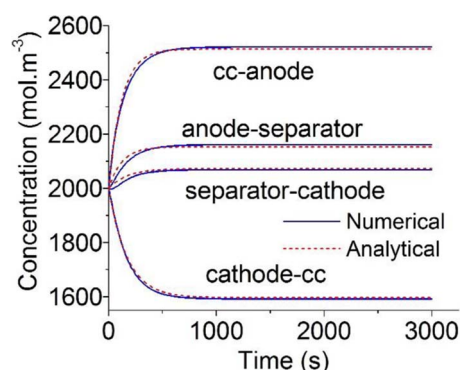


**Figure 3.** Comparison of concentrations that vary with time at selected interfaces for 1C charge rate.

because the coefficients  $a_k$  were derived based on steady-state conditions.

The electrolyte concentrations for a 1 C discharge as a function of time at the interface regions within a cell as shown in Fig. 3. The four selected interfaces are the interface between the current collector and the negative electrode, the interface between the negative electrode and the separator, the interface between the separator and the positive electrode, and the interface between the positive electrode and the current collector. As shown in Fig. 3, the concentration profiles at the electrode-current collector and electrode-separator interface agreed well ( $< 0.1\%$  error) with the numerical solution. Compared with similar second-order analytical solutions,<sup>22,25</sup> the model proposed in this paper improved the electrolyte profile in the positive electrode. At the electrode-current collector interface, the maximum concentration error is reduced from 2%<sup>22</sup> and 4%<sup>5</sup> to 0.8%, where the battery voltage is calculated from the electrolyte potential at this point. Further, when comparing the model based on the third-order solution,<sup>23</sup> this model and the model in Ref. 23 can accurately capture the physics of the electrolyte concentration at C-rates below 1 C. However, for higher C-rates, the voltage profile in Ref. 23 showed a maximum error of about 4% at a 5 C discharge with the volumetric mean flux, while the results of this study showed a 1.9% maximum error at a 5 C discharge with a simpler second-order expression. Additionally, this approximate solution can be applied to any type of operating condition, as well as the galvanostatic discharge condition.

In order to validate the model under dynamic loading, simulations of the Dynamic Stress Test (DST) and the Highway Fuel Economy Test (HWFET) were conducted. These tests are designed by the United States Advanced Battery Consortium to test EV and HEV batteries.<sup>37–39</sup> The electrolyte potential difference profiles for the DST and HWFET are plotted in Fig. 4. For the dynamic loading simulations, the initial electrolyte concentration was updated by the last value from the previous step (i.e.  $c_0 = c_e(x, 0)$  at  $t = 0$  and  $c_0 = c_e(x, t$

$\Delta t)$  at  $t \neq 0$ ) to capture the electrolyte concentration dynamic profile. Compared to the HWFET simulation, the DST simulation fluctuates less but have higher C-rate loads. Therefore, the error from electrolyte potential difference at high C-rates<sup>22</sup> will be more critical. For this reason, the errors will accumulate, leading to the deviation between the proposed SP and P2D models for the DST simulation. In general, Fig. 4 shows that the results from the proposed SP model agree well (average error  $< 0.03$  V) with those from the P2D model simulations. Therefore, the form for the approximate solution given by Eq. 31 is validated as being effective for the dynamic operating scenarios seen in EV and HEV applications. In summary, the approximate solution obtained in this study can be used to accurately describe the variation in the electrolyte concentration with respect to position and time for different operating scenarios.

**Cell voltage response.**—In this section, the cell voltage was simulated from 4.2 to 3 V for different C-rates (0.2 C, 1 C, 3 C, 5 C, and 10 C) based on Eqs. 5 and 31. The results were then compared with the P2D model results in Fig. 5. As shown in Figs. 5a and 5b, both the conventional and proposed SP models agree well with the P2D model results (0.0020 root mean square error (RMSE)) for a 0.2 C discharge rate. However, for higher C-rates, the proposed SP model results (with RMSE of 0.0048 for 1 C, 0.0249 for 3 C, 0.0379 for 5 C, and 0.1509 for 10 C) were much closer than the conventional SP results (RMSE of 0.0079 for 1 C, 0.0380 for 3 C, 0.0689 for 5 C, and 0.2766 for 10 C), as shown in Figs. 5c to 5j. The increased error at higher C-rates between the proposed SP and P2D models was because the electrolyte potential difference error increases with increasing C-rates as discussed in Proposed single particle model with electrolyte and stress-enhanced diffusion physics section. The uniform reaction distribution (Eqs. 1 and 4) used in the proposed SP model also differed from the results of the P2D model with non-uniform reaction distribution.<sup>22</sup> However, the proposed SP model reduced the average voltage error (shown in Table III) compared to the conventional SP model. In addition, with a short period of discharge time (at the beginning of discharge), the proposed model showed only a very small maximum error (0.01% to 0.21% for 0.2 C to 3 C), as compared to the rest of the discharge time. Thereby one of the shortcomings of the conventional SP model has been overcome. Modern batteries, especially for HEVs, can operate at more than 10 C, which is encountered during the DST.<sup>39,40</sup> The case of 10 C rate (Figs. 5g and 5h) demonstrated that the error rate increased considerably in the case of conventional SP model, as compared to the case of the proposed SP model. In conclusion, results for the proposed SP model were in good agreement with those from the P2D model. The voltage error was reduced considerably (reduced 39.98% RMSE), as compared to the voltage errors resulting from the conventional SP model.

The DST and HWFET were used to validate the proposed SP model for dynamic loads. As shown in Fig. 6, the proposed SP model for both the HWFET and the DST showed a considerable improvement in accuracy (reduced 55.8% RMSE for HWFET and 25% RMSE

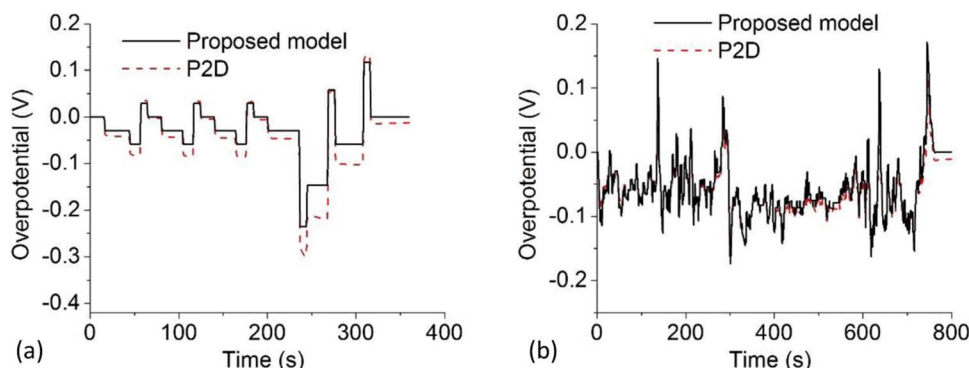


**Figure 4.** Electrolyte potential difference profile for (a) DST simulation and (b) HWFET simulation.

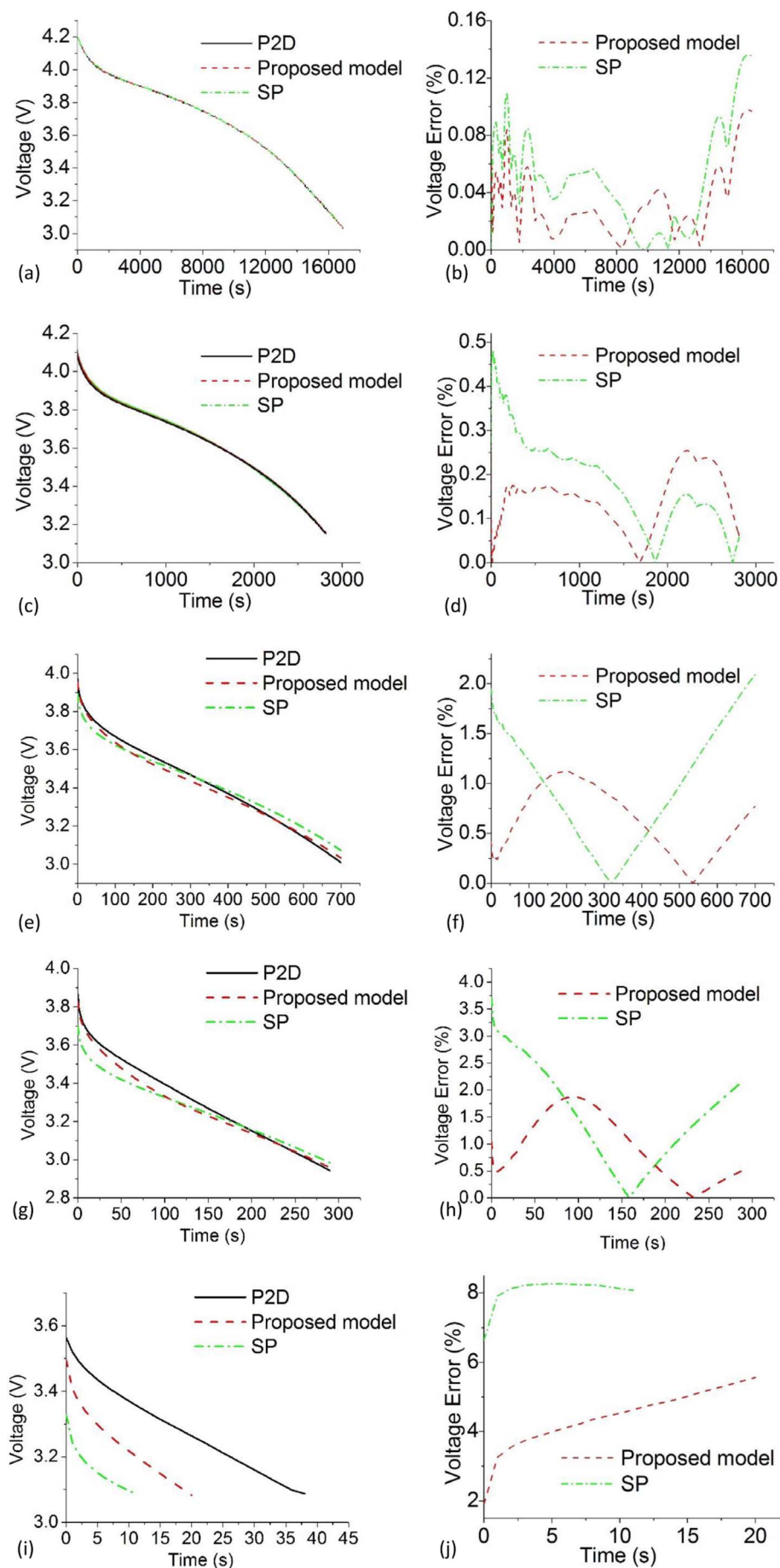


**Figure 5.** Comparison of time-dependent voltage responses and errors for P2D, SP, and proposed models for 0.2 C (a and b), 1 C (c and d), 3 C (e and f), 5 C (g and h), and 10 C (i and j) galvanostatic discharges.

**Table III.** Average error of proposed SP model and SP model.

Model	0.2 C (%)	1 C (%)	3 C (%)	5 C (%)	10 C (%)
SP	0.049 ± 0.035	0.183 ± 0.101	0.975 ± 0.574	1.533 ± 0.887	8.041 ± 0.434
Proposed model	0.032 ± 0.023	0.146 ± 0.064	0.630 ± 0.331	0.935 ± 0.608	4.417 ± 0.841

for DST) compared to the conventional SP model. As previously discussed, the proposed SP model was more accurate at short periods of discharge time and higher C-rates, as compared to the conventional SP model, indicating the proposed SP model is capable of accurately predicting cell voltage for dynamic loads.

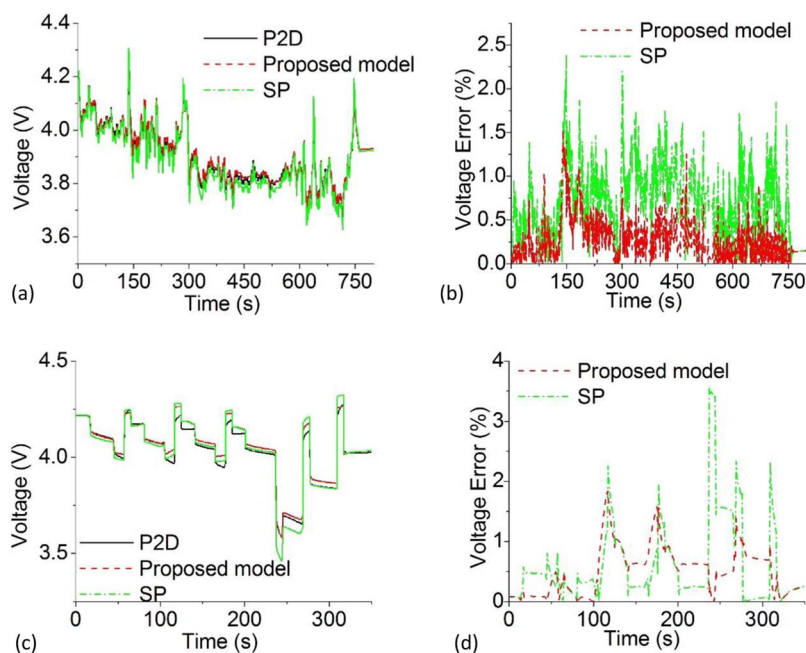
**Stress effects.**—Based on Eqs. 41 and 42, the stress model was coupled with the proposed SP model. In order to analyze the impact of stress on battery performance, three different galvanostatic discharge cases were conducted (i.e. 0.2, 1, and 3 C). The results for simulations using the proposed SP model, with and without coupling to the stress model, are shown in Fig. 7.

Including the stress model produced negligible effects (maximum error < 0.01 V) in the voltage profile for a 0.2 C discharge. However, as shown in Figs. 7c, 7d, 7i, and 7j, the voltage difference between the proposed SP model with and without stress increases with increasing C-rate, producing a maximum error of 0.16 V at the end of the 3 C discharge. In addition, the effect of stress on anode surface concentration was more pronounced when the C-rate was higher, as shown in Figs. 7c, 7g, and 7k. However, the difference in cathode surface concentration was negligible, even for high C-rates, as shown in Figs. 7d, 7h, and 7l. To demonstrate the applicability of the stress model in online estimation, the stress effect was added in the DST and HWFET loading conditions and as shown in Figs. 7m and 7n, different voltage responses were also observed depending on whether or not the stress effect was included.

Based on Eq. 42, it can be seen that stress increases diffusivity, leading to a considerable change in the anode surface concentration, thereby affecting the voltage responses. In Eq. 42, the diffusivity,  $D_{s,j}(1 + \theta_j C_{s,j}(r,t))$ , depends on the coefficient  $\theta_j$  and the li-ion concentration,  $C_{s,j}(r,t)$ , at each electrode,<sup>28</sup> and  $\theta_j$  depends on materials' mechanical properties. Various mechanical properties for  $\text{LiMn}_2\text{O}_4$  and  $\text{LiC}_6$  have been reported. For instance, the Young's modulus of  $\text{LiMn}_2\text{O}_4$  has been measured to be 25 GPa using a vibrating-reed measurement<sup>41</sup> and was measured to be 10 GPa using an elastic

spectroscopy.<sup>42</sup> The difference was due to the fact that the chemical composition of each sample was different.<sup>41,42</sup> Several battery modeling papers regarding  $\text{LiMn}_2\text{O}_4$ <sup>26,42</sup> have used a Young's modulus of 10 GPa that was measured using an elastic spectroscopy. In the present work, 10 GPa was selected because the target material was similar to that used in the reported experiment, and it was assumed that it was independent of the amount of lithium content. For the  $\text{LiMn}_2\text{O}_4$  cathode, the maximum increase in diffusivity is  $\theta_p \times C_{s,p,max} = 0.358$ , where  $\theta_p = 1.56 \times 10^{-5} \text{ m}^3/\text{mol}$  and  $C_{s,p,max} = 22,860 \text{ mol/m}^3$ . However, for the stiff graphite anode, the maximum increase in diffusivity is  $\theta_n \times C_{s,n,max} = 4.59$ , where  $\theta_n = 1.74 \times 10^{-4} \text{ m}^3/\text{mol}$  and  $C_{s,n,max} = 26,390 \text{ mol/m}^3$ . Therefore, the effect of stress on the anode diffusivity is much more significant than the effect of stress on the cathode diffusivity due to the order of magnitude difference in the coefficient,  $\theta_j$ . The difference of  $\theta_j$  is due to the difference at molar volume,  $\Omega_j$ , Young's modulus,  $E_j$ , as shown in Eq. 42 and Table I. The trend of the stress-diffusion coupling impact on battery performance is in agreement with the published results.

Diffusion-Induced Stress (DIS) and Stress-Enhanced Diffusion (SED) have been carefully studied and analyzed for decades.<sup>28,32,43–50</sup> Experimentally, as evidence of DIS, mechanical failures of active materials (such as cracking, fracture, and delamination) have been observed through different approaches, such as SEM,<sup>43–45</sup> AFM,<sup>45–47</sup> and other in situ observation methods.<sup>48,49</sup> For SED, most of the studies have been based on numerical simulations because it is difficult to decouple the effects of DIS and SED,<sup>28,32,45,50,51</sup> and a few of experimental studies were investigated the effect of stress on diffusivity<sup>52–53</sup> and on the battery voltage profile.<sup>54</sup> The coupled SED and DIS phenomenon were also analyzed by a finite deformation model, thereby accounting for the full coupling between diffusion and stress evolution.<sup>50</sup> Reference 50 indicated that SED would increase diffusion in the electrode and Ref. 28 also noted that considering SED effect would result in a lower concentration in the cathode during discharge due to the enhanced solid phase diffusivity. The observed impact of stress field on diffusivity and voltage profile (Fig. 7) in

**Figure 6.** Cell voltage profile and errors for P2D, SP, and proposed models for HWFET operating scenario (a and b) and DST operating scenario (c and d).



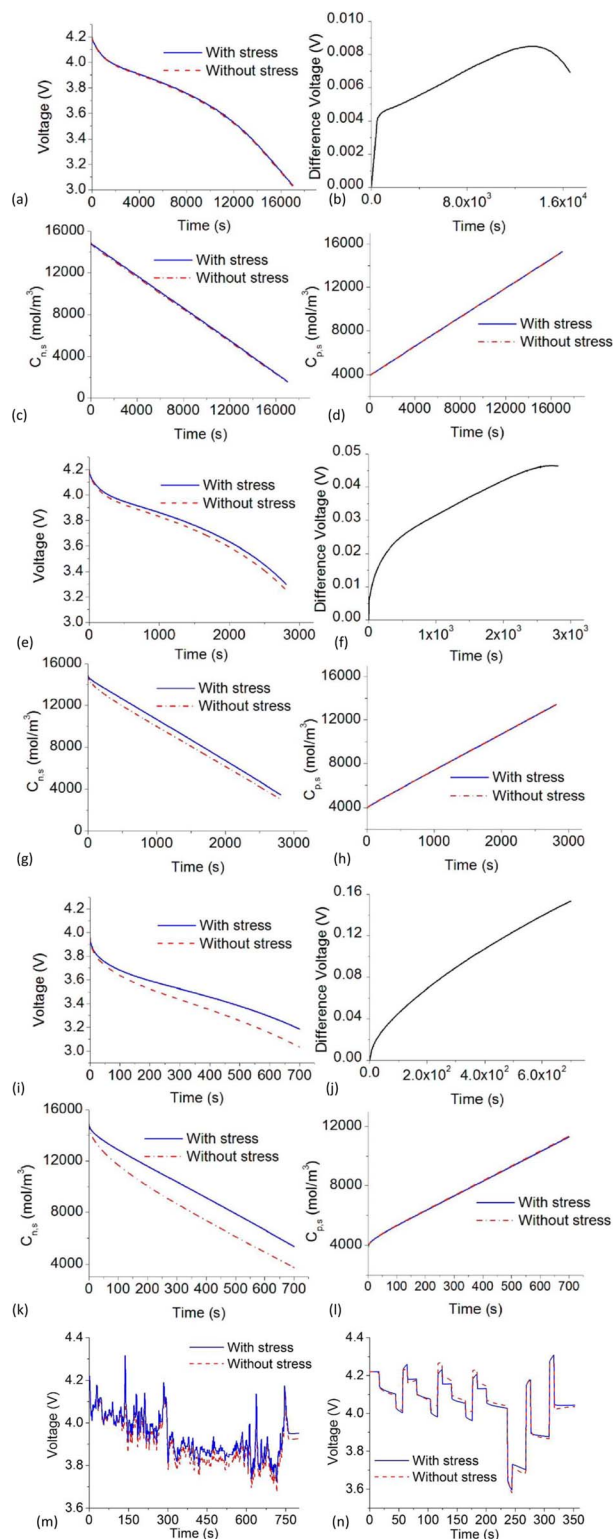


**Figure 7.** Comparison of proposed model with and without stress consideration (a) voltage comparison for 0.2 C, (b) difference with and without stress consideration for 0.2 C, (c) solid phase concentration in negative electrode surface for 0.2 C, and (d) solid phase concentration in positive electrode surface for 0.2 C; (e) voltage comparison for 1 C, (f) difference with and without stress consideration for 1 C, (g) solid phase concentration in negative electrode surface for 1 C, and (h) solid phase concentration in positive electrode surface for 1 C; (i) voltage comparison for 3 C, (j) difference with and without stress consideration for 3 C, (k) solid phase concentration in negative electrode surface for 3 C, and (l) solid phase concentration in positive electrode surface for 3 C; (m) voltage comparison for HWFET and (n) voltage comparison for DST.

this work agree quite well with the results in the literature,<sup>28,50</sup> in which the contribution of stress to diffusion was small at low lithium concentrations and SED became more pronounced as the lithium concentration increased. In conclusion, the proposed SP model, coupled with the stress model, indicated that it was necessary to consider an SED model capture the real battery physics governed by the coupling between stress and diffusion. This is especially important when using stiff materials or when operating at high charge and discharge rates as shown in Fig. 7.

## Conclusions

A low-order battery model was developed that incorporates stress-enhanced diffusion and electrolyte concentration distribution into a modified single particle model. An approximated analytical solution was derived for the electrolyte concentration distribution by solving the mass transport equation in the electrolyte of a li-ion cell. It has a simpler form than the P2D model and provided computational efficiency that is faster than that of the P2D model (almost 3 times faster in calculation time), and more accurate than that of the conventional SP model (reduced 33.8% average voltage error). It was confirmed that this approximate solution can be applied to any combination of operating scenarios, including constant charge/discharge, short/long interval, and rest period, as well as the dynamic loads.

From comparisons of the electrolyte concentration distributions and the potential difference profiles for various discharge conditions, it was concluded that the approximate solution is reliable and can be used to predict cell voltages with less than  $0.630 \pm 0.331\%$  voltage error for C-rates up to 3 C. In addition, coupling between the proposed SP model and a stress-model was considered. As a result, the effects of stress on cell voltage and solid phase concentrations was captured. The effect of stress has been found to non-negligible because it is important for medium to high C-rate operating conditions. Therefore, the proposed model considering both nonuniformly dispersive electrolyte and stress-enhanced diffusivity is more accurate than the conventional SP model for predicting cell voltage without losing computational efficiency.

## Acknowledgments

The authors acknowledge financial support from National Science Foundation Award No. CMMI-1538415.

## References

1. L. Lu, X. Han, J. Li, J. Hua, and M. Ouyang, *Journal of Power Sources*, **226**, 272 (2013).
2. V. Ramadesigan, P. W. Northrop, S. De, S. Santhanagopalan, R. D. Braatz, and V. R. Subramanian, *Journal of The Electrochemical Society*, **159**, R31 (2012).
3. D. Andrea, *Battery Management Systems for Large Lithium Ion Battery Packs*: Artech house, (2010).
4. M. Woon, X. Lin, A. Ivanco, A. Moskalik, C. Gray, and Z. Filipi, in *SAE 2011 World Congress and Exhibition*, (2011).
5. N. A. Chaturvedi, R. Klein, J. Christensen, J. Ahmed, and A. Kojic, *IEEE Control Systems*, **30**, 49 (2010).
6. R. Klein, N. A. Chaturvedi, J. Christensen, J. Ahmed, R. Findeisen, and A. Kojic, *American Control Conference*, 6618 (2010).
7. J. Prins-Jansen, J. D. Fehribach, K. Hemmes, and J. De Wit, *Journal of The Electrochemical Society*, **143**, 1617 (1996).
8. K. Smith and C. Y. Wang, *Journal of Power Sources*, **161**, 628 (2006).
9. M. W. Verbrugge and B. J. Koch, *Journal of The Electrochemical Society*, **150**, A374 (2003).
10. M. Doyle, T. F. Fuller, and J. Newman, *Journal of the Electrochemical Society*, **140**, 1526 (1993).
11. S. Santhanagopalan and R. E. White, *Journal of Power Sources*, **161**, 1346 (2006).
12. V. R. Subramanian, V. Boovaragavan, V. Ramadesigan, and M. Arabandi, *Journal of The Electrochemical Society*, **156**, A260 (2009).
13. X. Hu, S. Li, and H. Peng, *Journal of Power Sources*, **198**, 359 (2012).
14. "FreedomCAR battery test manual for power-assist hybrid electric vehicles", *US Department Of Energy/ID-11069*, (2003).
15. D. Dees, E. Gunen, D. Abraham, A. Jansen, and J. Prakash, *Journal of The Electrochemical Society*, **155**, A603 (2008).

16. M. Schlesinger, *Modeling and Numerical Simulations*, Springer-Verlag, New York, (2009).
17. G. Ning and B. N. Popov, *Journal of The Electrochemical Society*, **151**, A1584 (2004).
18. S. Santhanagopalan, Q. Guo, P. Ramadass, and R. E. White, *Journal of Power Sources*, **156**, 620 (2006).
19. V. R. Subramanian, V. D. Diwakar, and D. Tapriyal, *Journal of The Electrochemical Society*, **152**, A2002 (2005).
20. Q. Zhang and R. E. White, *Journal of Power Sources*, **165**, 880 (2007).
21. A. Guduru, P. W. Northrop, S. Jain, A. C. Crothers, T. R. Marchant, and V. R. Subramanian, *Journal of Applied Electrochemistry*, **42**, 189 (2012).
22. W. Luo, C. Lyu, L. Wang, and L. Zhang, *Microelectronics Reliability*, **53**, 797 (2013).
23. S. K. Rahimian, S. Rayman, and R. E. White, *Journal of Power Sources*, **224**, 180 (2013).
24. N. Baba, H. Yoshida, M. Nagaoka, C. Okuda, and S. Kawauchi, *Journal of Power Sources*, **252**, 214 (2014).
25. X. Han, M. Ouyang, L. Lu, and J. Li, *Journal of Power Sources*, **278**, 802 (2015).
26. J. Dahn, *Physical Review B*, **44**, 9170 (1991).
27. L. Beaulieu, S. Beattie, T. Hatchard, and J. Dahn, *Journal of The Electrochemical Society*, **150**, A419 (2003).
28. X. Zhang, W. Shyy, and A. M. Sastry, *Journal of The Electrochemical Society*, **154**, A910 (2007).
29. W. H. Woodford, Y. M. Chiang, and W. C. Carter, *Journal of The Electrochemical Society*, **157**, A1052 (2010).
30. K. Zhao, M. Pharr, J. J. Vlassak, and Z. Suo, *Journal of Applied Physics*, **108**, 073517 (2010).
31. J. Li, A. K. Dozier, Y. Li, F. Yang, and Y. T. Cheng, *Journal of The Electrochemical Society*, **158**, A689 (2011).
32. J. Park, W. Lu, and A. M. Sastry, *Journal of The Electrochemical Society*, **160**, X3 (2013).
33. Y. Qi, H. Guo, L. G. Hector, and A. Timmons, *Journal of The Electrochemical Society*, **157**, A558 (2010).
34. M. Guo, G. Sikha, and R. E. White, *Journal of The Electrochemical Society*, **158**, A122 (2011).
35. D. Di Domenico, A. Stefanopoulou, and G. Fiengo, *ASME Journal of Dynamic Systems, Measurement, and Control*, **132**, 061302 (2010).
36. E. Prada, D. Di Domenico, Y. Creff, J. Bernard, V. Sauvant-Moynot, and F. Huet, *Journal of The Electrochemical Society*, **159**, A1508 (2012).
37. C. Silva, M. Ross, and T. Farias, *Energy Conversion and Management*, **50**, 1635 (2009).
38. H. He, R. Xiong, and J. Fan, *Energies*, **4**, 582 (2011).
39. Electric vehicle battery test procedures manual, *U.S. Advanced Battery Consortium*, Southfield, MI, USA, (2006).
40. J. Wang, P. Liu, J. Hicks Garner, E. Sherman, S. Soukiazian, M. Verbrugge, H. Tataria, J. Musser, and P. Finamore, *Journal of Power Sources*, **196**, 3942 (2011).
41. J. Christensen and J. Newman, *Journal of The Electrochemical Society*, **153**, A1019 (2006).
42. X. Zhang, A. M. Sastry, and W. Shyy, *Journal of The Electrochemical Society*, **155**, A542 (2008).
43. M. R. Lim, W. I. Cho, and K. B. Kim, *Journal of Power Sources*, **92**, 168 (2001).
44. D. Wang, X. Wu, Z. Wang, and L. Chen, *Journal of Power Sources*, **140**, 125 (2005).
45. M. Chung, J. Seo, X. Zhang, and A. Sastry, *Journal of The Electrochemical Society*, **158**, A371 (2011).
46. J. Hun, M. Chung, M. Park, S. Woo, X. Zhang, and A. Marie, *Journal of The Electrochemical Society*, **158**, A434 (2011).
47. A. Clemencon, A. Appapillai, S. Kumar, and Y. Shao Horn, *Electrochimica Acta*, **52**, 4572 (2007).
48. V. A. Sethuraman, N. Van Winkle, D. P. Abraham, A. F. Bower, and P. R. Guduru, *Journal of Power Sources*, **206**, 334 (2012).
49. V. A. Sethuraman, M. J. Chon, M. Shimshak, V. Srinivasan, and P. R. Guduru, *Journal of Power Sources*, **195**, 5062 (2010).
50. Y. Gao and M. Zhou, *Journal of Applied Physics*, **109**, 014310 (2011).
51. R. Xu and K. Zhao, *Journal of Electrochemical Energy Conversion and Storage*, **13**, 030803 (2016).
52. K.B. McAfee Jr, *The Journal of Chemical Physics*, **28**, 218 (1958).
53. F. Célarié, M. Ciccotti, and C. Marliere, *Journal of Non-Crystalline Solids*, **353**, 51 (2007).
54. B. Lu, Y. Song, Q. Zhang, J. Pan, Y.T. Cheng, and J. Zhang, *Physical Chemistry Chemical Physics*, **18**, 4721 (2016).
55. A. Paolone, R. Cantelli, G. Rousse, and C. Masquelier, *Journal of Physics: Condensed Matter*, **15**, 457 (2003).